ACS Photonics

Article

pubs.acs.org/journal/apchd5

# Comparative Study of Second-Harmonic Generation from Epsilon-Near-Zero Indium Tin Oxide and Titanium Nitride Nanolayers Excited in the Near-Infrared Spectral Range

Antonio Capretti,[†,‡] Yu Wang,[†] Nader Engheta,[§] and Luca Dal Negro*[,†,∥]

[†]Department of Electrical and Computer Engineering and Photonics Center, Boston University, 8 Saint Mary's Street, Boston, Massachusetts 02215, United States

[‡]CNR-SPIN, Complesso MonteSantangelo, Via Cinthia, 80126 Napoli, Italy

[§]Department of Electrical and Systems Engineering, University of Pennsylvania, 200 South 33rd Street, Philadelphia, Pennsylvania 19104, United States

[∥]Division of Materials Science and Engineering, Boston University, 15 Saint Mary's Street, Brookline, Massachusetts 02446, United States

**ABSTRACT:** We perform a comparative study of second-harmonic generation (SHG) from indium tin oxide (ITO) and from titanium nitride (TiN) nanolayers excited in the near-infrared spectrum. Both materials are compatible with Si technology and are candidate platforms for integrated nonlinear optics. In this work, we fabricate ITO samples with an $\varepsilon$-near-zero (ENZ) condition, which can be continuously tailored in the 1150−1670 nm spectral range, and TiN samples with a metallic behavior in the same spectral range. For the ITO nanolayers, we observe tunability and enhancement of the SHG intensity when the samples are excited at their respective ENZ condition, in agreement with the electromagnetic modeling and analogous to its third-harmonic generation studied earlier. On the other hand, we show that the SHG efficiency of TiN nanolayers is lower by a factor of 50. We determine experimentally that the dominant component of the second-order susceptibility for our best ITO nanolayer is $\chi_{zzz}^{(2\omega)}$ = 0.18 pm V$^{-1}$, and we theoretically predict that the SHG process is enhanced up to 4 orders of magnitude when resonantly pumping the nanolayer at the ENZ wavelength with respect to a wavelength at 2000 nm. Remarkably, the resulting SHG efficiency is comparable with a crystalline quartz plate with thickness 0.5 mm used as a reference in our experiments in reflection configuration. Our study clearly indicates that ITO nanolayers with engineered ENZ conditions are a promising material platform for surface nonlinearities, with possible applications to nonlinear metasurfaces, Si-based flat optics, and sensing.

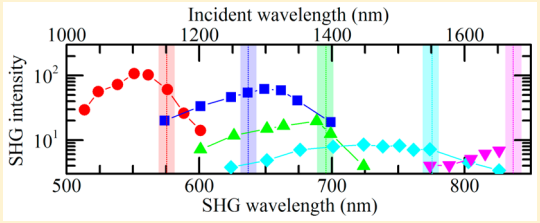


**KEYWORDS:** *epsilon-near-zero, indium tin oxide, titanium nitride, second-harmonic generation, thin film*

The recent advancements in the fields of plasmonics and metamaterials have stimulated the engineering of novel structures for relevant applications in optics.[1−3] Metamaterial analog signal processing has been introduced, based on multilayered slabs or subwavelength structured screens.[4] Ultrathin optical components, based on tailored modifications of phase to directly control light beams, have been demonstrated by means of flat metasurfaces.[5] Metamaterials made of digital units have been proposed as a general and powerful route to obtain desired electromagnetic properties.[6−8] Moreover, metal nanostructures have allowed the enhancement and the miniaturization of nonlinear optical processes by means of plasmonic resonances.[9,10] Chip-integrated electro-optic modulators have been obtained based on subwavelength localized plasmonic modes.[11,12] In brief, the proper combination of metal and dielectric constituents allows unique optical material properties and device performances. However, traditional noble metals, such as Au and Ag, suffer from high extinction losses in the optical and near-infrared spectrum[13] due to both interband electronic transitions and conduction losses. Consequently, metal nanostructures show structural and thermal instabilities under strongly confined electromagnetic fields. This is especially critical for nonlinear optical applications, where ultrafast light pulses are used as the excitation light.[14−16] Moreover, noble metals suffer from very limited processing compatibility with respect to the widespread Si microfabrication technology.

In order to solve these problems, conductive oxides and nitride-based materials have been explored in recent years as alternative tunable platforms for the engineering of plasmonic resonances and for the design of metamaterials in the near-infrared spectral range.[17−22] Such materials have a higher melting point than noble metals, they are chemically stable at high temperatures,[23,24] and consequently, they can withstand more intense electromagnetic fields. Specifically, indium tin oxide (ITO) is a conductive oxide largely utilized as a transparent contact, while titanium nitride (TiN) is utilized as

**Received:** June 28, 2015
**Published:** October 5, 2015





DOI: 10.1021/acsphotonics.5b00355
*ACS Photonics* 2015, 2, 1584−1591

a coating material and as a conductive barrier.[25,26] Both materials are compatible with the fabrication standards of the Si microelectronic industry.

Among the wide range of investigated metamaterials, optical media exhibiting the $\varepsilon$-near-zero (ENZ) condition are strongly pursued due to their unique properties.[27] They have been proposed to control the propagation and localization of electromagnetic fields with applications to energy squeezing,[28,29] imaging,[30] light trapping,[31] and scattering.[32,33] Moreover, the enhancement of the normal component of the electric field inside ENZ media was theoretically predicted and proposed as a convenient strategy to enhance nonlinear harmonic generation,[34−36] to boost optical bistability in Kerr nonlinear devices,[37] and to realize better optoelectronic switchers.[38] More recently, the nonlinear optical properties of ENZ media have been experimentally investigated and phase mismatch-free propagation has been demonstrated.[39] Typically, ENZ media are obtained at optical frequencies by means of three-dimensional nanomanufacturing, utilizing metal components.[40−42] Lately, our group investigated the optical properties of Si-compatible ITO nanolayers and utilized the tunable ENZ condition in the near-infrared to experimentally demonstrated strong enhancement of third harmonic generation (THG).[43] In particular, we showed that by resonantly pumping ITO nanolayers at their ENZ condition, a third-harmonic efficiency ~600× higher than crystalline Si can be achieved.

## RESULTS AND DISCUSSION

ITO and TiN are currently being extensively investigated as alternative components for metamaterials.[17−20,23,24] In the present work, we investigate the potential of both ITO and TiN materials as platforms for second-order optical nonlinearities. Specifically, we fabricate ITO nanolayers featuring a tailorable ENZ condition in the near-infrared, and we experimentally demonstrate enhanced second-harmonic generation (SHG) due to their ENZ response. Moreover, we investigate the SHG properties of TiN nanolayers with a metallic behavior in the same spectral range. The results of our comparative study show that the SHG from the ITO nanolayers is 50× more efficient than TiN, with an intensity comparable to that of a crystalline quartz plate of thickness 0.5 mm, used as a reference. Eventually, we quantify the second-order susceptibility of the fabricated samples by using the rigorous Green-function formalism for surface optics.

**Sample Deposition and Annealing Processes.** We use RF magnetron sputtering to deposit ITO thin films on Si substrate from an ITO target in Ar atmosphere, as detailed in refs 43 and 44. Similarly, we deposit TiN thin films using DC reactive sputtering, from a Ti target in $N_2$ atmosphere, with a gas flow at 10 sccm. The thickness of the fabricated samples is fixed at approximately 37 ± 5 nm for ITO and 40 ± 5 nm for TiN. In order to tailor the optical properties of the fabricated samples, we perform postdeposition thermal annealing processes, with increasing annealing time and temperature, as detailed in Table 1 for ITO and in Table 2 for TiN. We measure the electric permittivity $\varepsilon(\omega)$ of all the fabricated samples by using variable angle spectroscopic ellipsometry. The postdeposition annealing processes results in a large tunability of the optical dispersions for both materials.

**Ellipsometric Characterization.** The ellipsometric data for all the ITO and TiN nanolayers are fitted with a very good accuracy using the standard Drude-Sommerfeld model for the free charge carriers:

**Table 1. Fabrication Parameters for ITO Nanolayers**

| $\lambda_{ENZ}$ (nm) | $\lvert\varepsilon\rvert = \varepsilon''$@ $\lambda_{ENZ}$ | anneal. temp. (°C) | anneal. time (min) | ramp-up time (s) |
|---|---|---|---|---|
| 1150 | 0.53 | 750 | 60 | 15 |
| 1270 | 0.52 | 750 | 30 | 15 |
| 1390 | 0.48 | 550 | 30 | 15 |
| 1550 | 0.61 | 350 | 60 | 15 |
| 1670 | 0.54 | 350 | 30 | 15 |

**Table 2. Fabrication Parameters for TiN Nanolayers**

| $\lambda_{ps}$ (nm) | $\lvert\varepsilon\rvert = \varepsilon''$@ $\lambda_{ps}$ | anneal. temp. (°C) | anneal. time (min) | ramp-up time (min) |
|---|---|---|---|---|
| 510 | 3.10 | 900 | 60 | 1 |
| 545 | 3.55 | 800 | 60 | 1 |
| 565 | 3.65 | 700 | 60 | 1 |
| 615 | 5.07 | 500 | 60 | 1 |
| 640 | 6.51 | 300 | 60 | 1 |
| 645 | 8.12 | as deposited | | |

$$\varepsilon(\omega) = \varepsilon'(\omega) + i\varepsilon''(\omega) = \varepsilon_\infty - \frac{\omega_p^2}{\omega^2 + i\Gamma\omega} \quad (1)$$

where $\omega_p$ is the plasma angular frequency and $\Gamma$ is the collision rate of the carriers. Here, $\varepsilon_\infty$ represents the background permittivity, which accounts for the effects of the electron transitions occurring at higher frequencies. In the Drude-Sommerfeld model, the zero of the real permittivity $\varepsilon' = 0$ is generally referred as screened plasma wavelength $\lambda_{ps}$, which is given by the relation $(2\pi c/\lambda_{ps})^2 = \omega_p^2/\varepsilon_\infty - \Gamma^2$. In the following, we also define an ENZ condition as the minimum of the absolute permittivity $|\varepsilon(\omega)| = |\varepsilon'(\omega) + i\varepsilon''(\omega)|$, with the necessary requirement that $|\varepsilon(\omega)| < 1$. Differently from the screened plasma wavelength, this condition guarantees the enhancement of the normal component of the internal electric field, which drives the unique properties of the ENZ media. For the simple model in eq 1, the ENZ condition corresponds with the screened plasma wavelength $\lambda_{ps}$, only if the imaginary permittivity is less than unity ($|\varepsilon(\omega)| = \varepsilon'' < 1$).

The experimental complex permittivity $\varepsilon(\omega)$ is shown in Figure 1, with the real part $\varepsilon'$ on the left column and the imaginary part $\varepsilon''$ on the right column. The permittivity of the ITO nanolayers is shown in Figure 1a,b. These samples feature a $\lambda_{ENZ}$ in the range between 1150 and 1670 nm, demonstrating that the ENZ condition can be largely tailored with the postdeposition annealing process. At the ENZ wavelength, the absolute permittivity $|\varepsilon(\omega)| = \varepsilon''$ is in the range 0.48−0.61, which is much smaller than noble metals in the targeted infrared spectrum.[45] The permittivity of the TiN nanolayers is shown in Figure 1c,d. The fabricated TiN samples show a screened plasma wavelength that is tailored in the visible spectrum between 510 and 645 nm. The absolute permittivity $|\varepsilon(\omega)| = \varepsilon''$ at the ENZ wavelength is larger than unity for all samples.

**Calculated Internal Electric Field.** We performed accurate electromagnetic calculations in order to quantify the electric field inside the fabricated nanolayers at the excitation wavelength, which drives the optical nonlinearities investigated in this article.[46] Specifically, we considered a free-space ($m$ = 0)/nanolayer ($m$ = 1)/substrate ($m$ = 2) geometry illuminated by an incident plane wave with wavevector $\mathbf{k}_0$ lying in the $xOz$ plane. We adopt the same spatial coordinates as in ref 46 with the $\hat{\mathbf{z}}$-axis perpendicular to the layer surface (the interface



DOI: 10.1021/acsphotonics.5b00355
ACS Photonics 2015, 2, 1584−1591

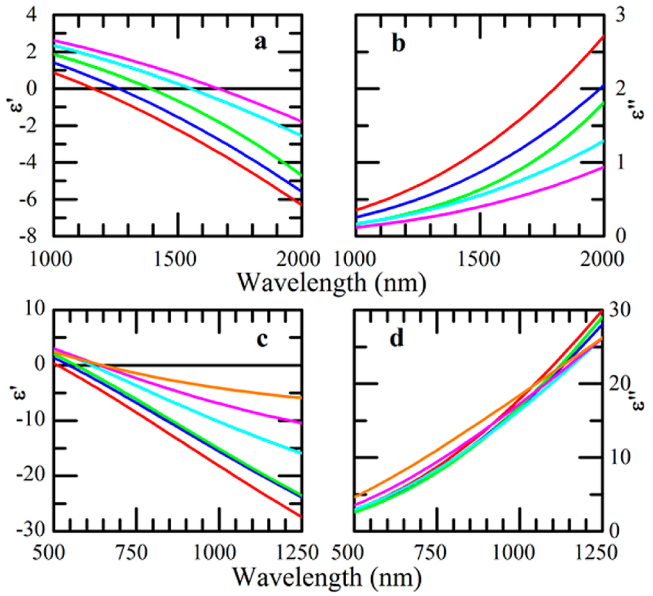


**Figure 1.** Real part $\varepsilon'$ (a) and imaginary part $\varepsilon''$ (b) of the electric permittivity for the ITO nanolayers with $\lambda_{ENZ}$ = 1150 (red), 1270 (blue), 1390 (green), 1550 (cyan), and 1670 nm (magenta). Real part $\varepsilon'$ (c) and imaginary part $\varepsilon''$ (d) of the electric permittivity for the TiN nanolayers with $\lambda_{ps}$ = 510 (red), 545 (blue), 565 (green), 615 (cyan), 640 (magenta) and 645 nm (orange).

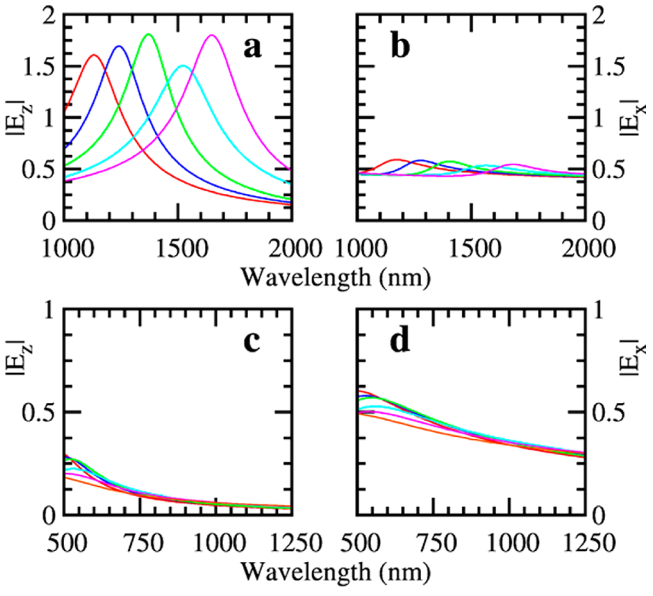


**Figure 2.** Amplitude of the internal electric field components $E_z$ (a) and $E_x$ (b) as a function of the incident wavelength, for the ITO nanolayers with $\lambda_{ENZ}$ = 1150 (red), 1270 (blue), 1390 (green), 1550 (cyan), and 1670 nm (magenta); $E_z$ (c) and $E_x$ (d) for the TiN nanolayers with $\lambda_{ps}$ = 510 (red), 545 (blue), 565 (green), 615 (cyan), 640 (magenta), and 645 nm (orange).

between the free-space and the nanolayers is at $z = -d_1 = 0$, while the interface between the nanolayer and the substrate is at $z = -d_2 = -D$). Similarly to what we did in ref 43, here we express the electric field in the generic medium $m$ as

$$\mathbf{E}_m(x, y, z) = A_m^{TE}[1 + \tilde{R}_{m,m+1}^{TE} e^{2ik_{m,z}(d_m+z)}]e^{i(k_{m,x}x - k_{m,z}z)}\hat{\mathbf{y}} \quad (2)$$

$$\mathbf{E}_m(x, y, z) = \zeta_m A_m^{TM}\left[\frac{k_{m,z}}{k_m}(1 - \tilde{R}_{m,m+1}^{TM} e^{2ik_{m,z}(d_m+z)})\hat{\mathbf{x}} + \frac{k_{m,x}}{k_m}(1 + \tilde{R}_{m,m+1}^{TM} e^{2ik_{m,z}(d_m+z)})\hat{\mathbf{z}}\right]e^{i(k_{m,x}x - k_{m,z}z)} \quad (3)$$

where eq 2 is for the case of s-polarized incident plane wave, and eq 3 for the case of p-polarization. The generic medium $m$ is characterized by its wavenumber $k_m$ and impedance $\zeta_m$. The spatial components of the wavevector $\mathbf{k}_m$ in medium $m$ (indicated by the $x,y,z$ subscripts) are determined by the Snell's law. The complete expressions for the coefficients $A_m$ and $\tilde{R}^{m,m+1}$ are well-known for both $s$- and $p$-polarizations.[46] In this work, the fields are normalized with respect to the amplitude of the incident electric field $|\mathbf{E}_{inc}|$ (i.e., we assume $A_0^{TE} = 1$ and $A_0^{TM} = \zeta_0^{-1}$). We used the experimental values of the permittivity obtained from our ellipsometric data to calculate the amplitude of the electric field $\mathbf{E}_1$ inside the fabricated nanolayers, when the incident wave is p-polarized (for simplicity we will drop the subscript 1). The results are displayed in Figure 2a,b for ITO and in Figure 2c,d for TiN. The field amplitude and phase are, with good approximation, constant along the nanolayer thickness, due to their subwavelength extent. Here, the normal ($E_z$) and the tangent ($E_x$) components of the field calculated at the interface with free space ($z = 0$).

We already showed in ref 43 that the normal component $E_z$ inside the ITO nanolayers has a maximum in correspondence with the ENZ wavelength, at incident angles in the range 45−55° with respect to the surface normal. This angle corresponds to the quasi-Brewster mode,[47] whose dispersion is described by the upper polariton branch of the investigated layered material. All the calculations in Figure 2 are performed at an incident angle of 45°. The normal component $E_z$ inside the ITO nanolayers is shown in Figure 2a and it is maximized at the ENZ wavelength for each investigated sample. For the ITO nanolayers the amplitude of $E_z$ is larger than the incident electric field by a factor between 1.5 and 1.8. In Figure 2b, we show the amplitude of the tangent component $E_x$ that, contrary to the normal component, is considerably reduced with respect of the incident field by a factor ∼0.5. The $E_z$ and $E_x$ components of the electric field inside the TiN samples are shown in Figure 2c,d, respectively. For all the fabricated samples, both components are reduced with respect of the incident field. The $E_x$ component dominates over the $E_z$ component by a factor ∼2, due to the metallic behavior of the TiN samples in the investigated spectral range. For each TiN sample, the electric field in the TiN samples slightly increases in proximity of the screened plasma wavelength $\lambda_{ps}$. However, both field components remains lower than the incident field, due to the high material losses (see Table 2).

**Second-Harmonic Generation Spectroscopy.** The calculations of the internal electric field in the previous section pointed out the different behavior of the ITO and of the TiN nanolayers in the investigated near-infrared regime. In the following we experimentally characterize the nonlinear optical responses of the fabricated samples using SHG spectroscopy. Figure 3a shows a schematic of the experimental setup, which utilizes an Optical Parametric Oscillator (OPO, Inspire Auto 100, Spectra-Physics) pumped by a Ti:sapphire laser (Mai Tai, Spectra-Physics), delivering ultrafast pulses of 150 fs duration at a 81 MHz repetition rate. We use as the excitation beam the OPO idler output, scanning the 1000−1700 nm spectral range. A 1000 nm long-pass filter (LPF) removes any spurious signal from the excitation beam, which is modulated by a mechanical chopper (C) and has an average power of 10 mW. A 20×


DOI: 10.1021/acsphotonics.5b00355
ACS Photonics 2015, 2, 1584−1591

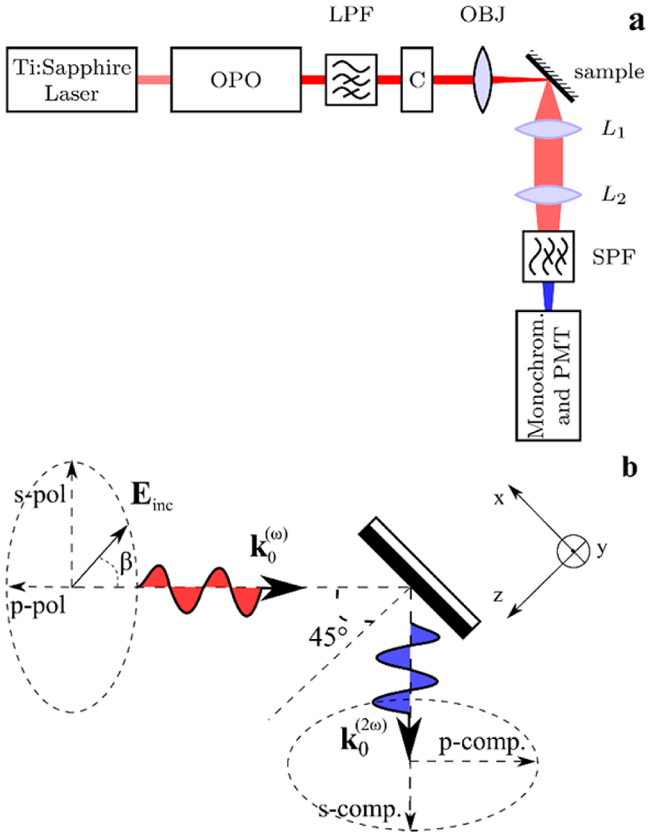


**Figure 3.** (a) SHG experimental setup. (b) Polarization configuration for both the excitation beam and the reflected SHG.

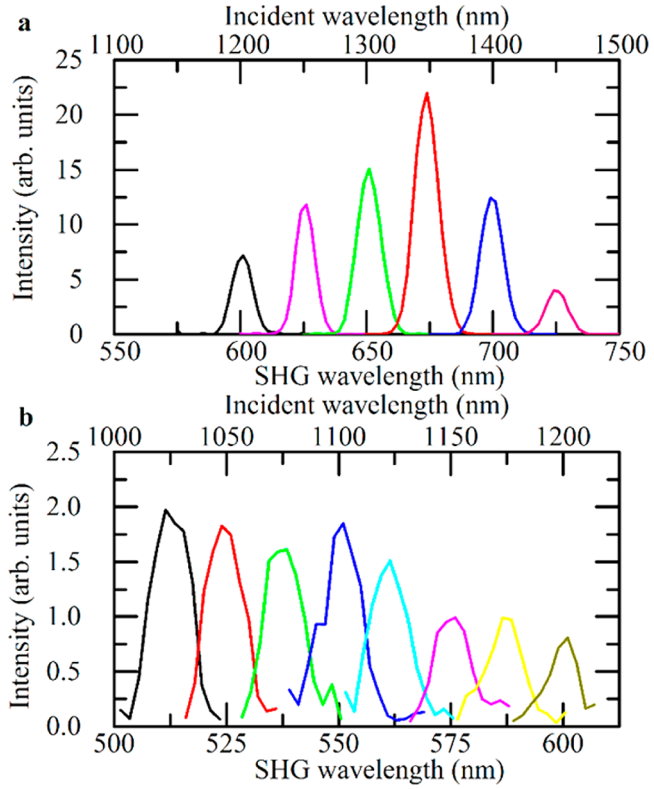


**Figure 4.** (a) SHG signals of the ITO nanolayer with $\lambda_{ENZ}$ = 1390 nm at incident wavelength $\lambda$ = 1200 (black), 1250 (magenta), 1300 (green), 1350 (red), 1400 (blue), and 1450 nm (pink). (b) SHG signals of the TiN nanolayer with $\lambda_{ps}$ = 545 nm at incident wavelength $\lambda$ = 1025 (black), 1050 (red), 1075 (green), 1100 (blue), 1125 (cyan), 1150 (magenta), 1175 (yellow), and 1200 nm (dark yellow).

microscope objective (OBJ) focuses the beam onto the sample under investigation, resulting in a peak intensity in the focused beam spot of approximately $I_{peak}^{(\omega)}$ = 42 MW/cm$^2$. The incident angle is 45° for all the acquisitions, and the SHG signal is collected in reflection configuration through a 30 mm lens (L1). The collected light is then coupled into a monochromator (Cornerstone 260, Newport) through a 180 mm lens (L2). A 1000 nm short-pass filter (SPF) is placed in front of the monochromator slits to reject the excitation wavelength. The SHG spectra have been detected with a lock-in amplifier (M-70100, Oriel Merlin) coupled to a low-light photomultiplier tube (PMT, 77348 Oriel Instrumentation). Figure 3b shows a schematic of the polarization configuration for both the excitation (red) and the collected SHG signal (blue). The excitation beam is linearly polarized, and the polarization is defined by the angle $\beta$, such that $\beta$ = 0° determines an incident *p*-polarization and $\beta$ = 90° an incident *s*-polarization.

With the experimental setup described above, the ITO nanolayers are excited in the spectral range of their $\lambda_{ENZ}$. On the contrary, the TiN samples are excited in a spectral range where their response is metallic, and the SHG signal is generated in proximity of their screened plasma wavelength $\lambda_{ps}$. For these reasons, the fabricated ITO and TiN materials represent a complementary choice to investigate the SHG processes while scanning the incident wavelength in the near-infrared. In Figure 4a we show representative SHG spectra collected under *p*-polarized incidence ($\beta$ = 0°) for the ITO sample with $\lambda_{ENZ}$ = 1390 nm. Analogously to our THG case reported in ref 43, the intensity exhibits a maximum at the incident wavelength around $\lambda_{ENZ}$. In Figure 4b we show representative SHG spectra collected under *p*-polarized incidence for the TiN sample with $\lambda_{ps}$ = 545 nm. In this case, the SHG signal is very low and it is close to the noise background of our experimental configuration. The SHG intensity grows monotonically when the incident wavelength is reduced from 1200 to 1000 nm. As a normal practice, we substitute the investigated samples with their substrate, in order to show that the SHG signals are indeed generated inside the fabricated ITO and TiN nanolayers. No SHG signal is detected under the same excitation conditions in the substrate.

The SHG intensities are summarized in Figure 5 for all the investigated samples. Figure 5a displays the case of the ITO nanolayers, showing a characteristic trend that approximately peaks at the corresponding $\lambda_{ENZ}$ for each sample, similarly to what we previously reported for the third-harmonic generation.[43] The small discrepancy between the $\lambda_{ENZ}$ and the peak of the SHG signal is attributed to the finite scanning accuracy (25 nm) that we used to tune the pump wavelength in the SHG experiments. This data confirms that the control of the ENZ condition in homogeneous ITO nanolayers allows reliable tuning of their second-order nonlinear optical properties in a wide spectral range, which is interesting for telecommunication applications. The behavior of the SHG intensity with respect to the incident wavelength has been investigated for all the TiN nanolayers. The samples annealed at temperatures lower than 700 °C show no detectable SHG signal. For all the remaining samples, the SHG intensity increases as the incident wavelength decreases, as summarized in Figure 5b. Remarkably, the maximum achieved SHG efficiency for the TiN nanolayers is a factor of 50 lower than the best ITO nanolayer. The trends of



DOI: 10.1021/acsphotonics.5b00355
*ACS Photonics* 2015, 2, 1584−1591

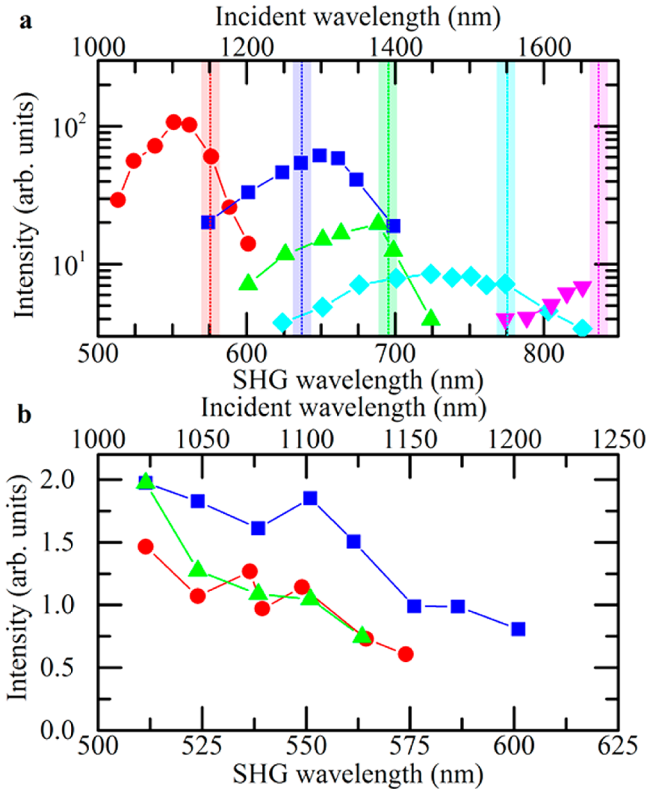


**Figure 5.** (a) SHG intensity as a function of the incident wavelength for the ITO nanolayers with $\lambda_{ENZ}$ = 1150 (red), 1270 (blue), 1390 (green), 1550 (cyan), and 1670 nm (magenta). The vertical lines mark the $\lambda_{ENZ}$ for each sample. The widths of the stripes indicate the scanning accuracy of the pump wavelength. (b) SHG intensities as a function of the incident wavelength for the TiN nanolayer with $\lambda_{ps}$ = 510 (blue), 545 (green), and 565 nm (red).

the SHG intensity are consistent with the electric field calculations previously discussed, for both ITO and TiN materials.

**Second-Order Susceptibility.** The components of the second-order susceptibility can be determined by measuring the dependence of the SHG intensity on the polarization of the incident beam. Specifically, we performed SHG measurements for both *s*- and *p*- detection configurations as a function of the angle of polarization $\beta$ of the incident beam. In this experiment, the incident beam polarization is rotated by using a $\lambda/4$ waveplate followed by a Glan-Laser polarizer. The incident polarization is defined by the angle $\beta$, such that $\beta = 0°$ determines a *p*-polarization and $\beta = 90°$ a *s*-polarization. The collected SHG signal is analyzed in its *p*- and *s*-components by a polarizer. In Figure 6a,b, the collected SHG *p*-and *s*-components are shown versus $\beta$ for the representative ITO sample excited at its ENZ wavelength $\lambda_{ENZ}$ = 1150 nm. We notice that the intensity of the SHG *s*-component is zero for both *p* ($\beta = 0°$) and *s* ($\beta = 90°$) incident polarizations. This follows from the fact that the fabricated films possess in-plane isotropy ($C_{\infty v}$ symmetry group). Consequently, there are three allowed and independent components for the second-order susceptibility: namely $\chi^{(2\omega)}_{zzz}$, $\chi^{(2\omega)}_{zxx} = \chi^{(2\omega)}_{zyy}$, and $\chi^{(2\omega)}_{xzx} = \chi^{(2\omega)}_{xxz} = \chi^{(2\omega)}_{yzy} = \chi^{(2\omega)}_{yyz}$. Moreover, the SHG *p*-component is zero for the *s* ($\beta = 90°$) incident polarization, and the $\chi^{(2\omega)}_{zxx} = \chi^{(2\omega)}_{zyy}$ component is negligible. Here, the maximum intensity of the SHG *p*-component (at $\beta = 0°$) is approximately 20× more intense than the *s*-component (at $\beta = 45°$). In conclusion, the

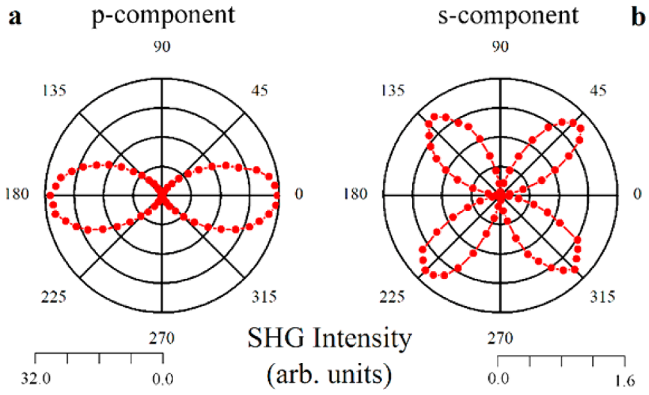


**Figure 6.** Intensity of the SHG *p*- (a) and *s*- (b) components as a function of the polarization angle of the incident beam $\beta$ for the ITO nanolayer with $\lambda_{ENZ}$ = 1150 nm at incident wavelength $\lambda = \lambda_{ENZ}$.

two relevant components of the second-order susceptibility are $\chi^{(2\omega)}_{zzz}$ and $\chi^{(2\omega)}_{xzx}$ for both materials. This result confirm that the SHG signal is mainly driven by the normal component $E_z$ of the electric field. It has not been possible to conduct a similar analysis for the TiN samples with the same experimental apparatus, due to their low SHG intensity.

In order to further confirm the effect of the ENZ-enhancement of the electric field over the SHG process, we calculate the SHG intensity as a function of the excitation wavelength for all the fabricated samples. We fix the incident polarization at $\beta = 0°$ (*p*-polarization) and the incident angle at 45°, as in the experimental section discussed previously. We consider the same multilayer planar geometry as before, where an incident plane wave illuminates the structure from free-space, inducing a second-order nonlinear bulk polarization $\mathbf{P}^{(2\omega)}$ inside the nanolayer:

$$\mathbf{P}^{(2\omega)} = \varepsilon_0 \vec{\vec{\chi}}^{(2\omega)} : \boldsymbol{EE} \tag{4}$$

where $\vec{\vec{\chi}}^{(2\omega)}$ is the bulk second-order susceptibility and $\boldsymbol{E}$ is the electric field inside the nanolayer (we dropped the subscript 1) calculated at the excitation wavelength from eqs 2 and 3. The SHG field reflected back to free space can be expressed by using the rigorous Green-function formalism for surface optics:[48,49]

$$E_r^{(2\omega)} = \frac{i}{2}\frac{k_0^{(2\omega)^2}}{k_{1,z}^{(2\omega)}}\frac{t_{10}^{(2\omega)}}{1 - r_{12}^{(2\omega)} r_{10}^{(2\omega)} e^{2ik_{1,z}^{(2\omega)}D}} \times \int_{-D}^{0} (e^{-k_{1,z}^{(2\omega)}z'}\hat{\mathbf{q}}_{1+}^{(2\omega)} + r_{12}^{(2\omega)} e^{2ik_{1,z}^{(2\omega)}D} e^{k_{1,z}^{(2\omega)}z'}\hat{\mathbf{q}}_{1-}^{(2\omega)}) \cdot \frac{\mathbf{P}^{(2\omega)}}{\varepsilon_0} dz' \tag{5}$$

where the subscripts $m$ = 0, 1, and 2 are the same as in the previous sections, and all the quantities with the $(2\omega)$ superscript are related to the second-harmonic fields: $k_0^{(2\omega)}$ is the free-space wavenumber, $k_{1,z}^{(2\omega)}$ is the *z*-component of the wavevector inside the nanolayer, $t_{ij}^{(2\omega)}$ and $r_{ij}^{(2\omega)}$ are the Fresnel transmission and reflection coefficients for the electric field at the interface between two media *i* and *j* (the appropriate coefficient have to be selected for *p*- and *s*-polarizations), $\hat{\mathbf{q}}_{1\pm}^{(2\omega)}$ describes the polarization state of the generated light (as defined in ref 48). The integration variable $z'$ goes from $-D$ (corresponding to the interface between the nanolayer and the substrate) to 0 (corresponding to the interface between the free-space and the nanolayer) in the coordinate system adopted throughout this manuscript. Given the subwavelength thickness



DOI: 10.1021/acsphotonics.5b00355
ACS Photonics 2015, 2, 1584−1591

of the investigated nanolayers, we assume that $k_{1,z}^{(2\omega)} \ll 1$ and that the **E** field is constant along the $z$ direction. Consequently, the second-order bulk polarization $\mathbf{P}^{(2\omega)}$ is constant across the nanolayers thickness, and eq 5 can be approximated as

$$E_r^{(2\omega)} = \frac{i}{2}\frac{k_0^{(2\omega)^2} D}{k_{1,z}^{(2\omega)}} \frac{t_{10}^{(2\omega)}}{1 - r_{12}^{(2\omega)} r_{10}^{(2\omega)} e^{2ik_{1,z}^{(2\omega)} D}} \times (\hat{\mathbf{q}}_{1+}^{(2\omega)} + r_{12}^{(2\omega)} e^{2ik_{1,z}^{(2\omega)} D} \hat{\mathbf{q}}_{1-}^{(2\omega)}) \cdot \frac{\mathbf{P}^{(2\omega)}}{\varepsilon_0}\Big|_{z=0} \quad (6)$$

where $\mathbf{P}^{(2\omega)}$ is calculated inside the nanolayer, at the interface with free-space.

The calculated SHG intensity is shown in Figure 7 for the ITO nanolayers, as a function of the incident wavelength. This calculation is performed for each of the allowed second-order susceptibility components separately from the others. In Figure 7a, we used the set of parameters ($\chi_{zzz}^{(2\omega)} \neq 0$, $\chi_{xzx}^{(2\omega)} = 0$, $\chi_{zxx}^{(2\omega)} = 0$). Analogously, we used the set of parameters ($\chi_{zzz}^{(2\omega)} = 0$, $\chi_{xzx}^{(2\omega)} \neq 0$, $\chi_{zxx}^{(2\omega)} = 0$) for Figure 7b and ($\chi_{zzz}^{(2\omega)} = 0$, $\chi_{xzx}^{(2\omega)} = 0$, $\chi_{zxx}^{(2\omega)} \neq 0$) for Figure 7c. Each of the allowed components of $\overleftrightarrow{\chi}^{(2\omega)}$ exhibit maximum SHG generation when the samples are pumped at the $\lambda_{ENZ}$, in agreement with the experimental results showed in Figure 5. However, the width of the SHG peak is shorter for the $\chi_{zzz}^{(2\omega)}$ component in Figure 7a, and it increases for $\chi_{xzx}^{(2\omega)}$ in Figure 7b. The bandwidth further increases for the $\chi_{zxx}^{(2\omega)}$, which also features a much shorter SHG intensity. These results are easily explained by considering the amplitude of the $E_z$ and $E_x$ components shown in Figure 2. We notice that for the $\chi_{zzz}^{(2\omega)}$ component shown in Figure 7a, our calculations predict a SHG intensity enhanced by approximately 4 orders of magnitude, compared to wavelengths detuned from the ENZ condition. It is also important to note that the SHG from the fabricated ITO nanolayers benefits from both from the enhanced electric field of the excitation and from the improved extraction of the SHG light. As a matter of fact, the fabricated ITO samples are transparent in the visible spectrum.

We performed a similar analysis for the TiN nanolayers. Figure 8 shows the calculated SHG intensity as a function of the incident wavelength. In Figure 8a, we used the set of parameters ($\chi_{zzz}^{(2\omega)} \neq 0$, $\chi_{xzx}^{(2\omega)} = 0$, $\chi_{zxx}^{(2\omega)} = 0$). Analogously, we used the set of parameters ($\chi_{zzz}^{(2\omega)} = 0$, $\chi_{xzx}^{(2\omega)} \neq 0$, $\chi_{zxx}^{(2\omega)} = 0$) for

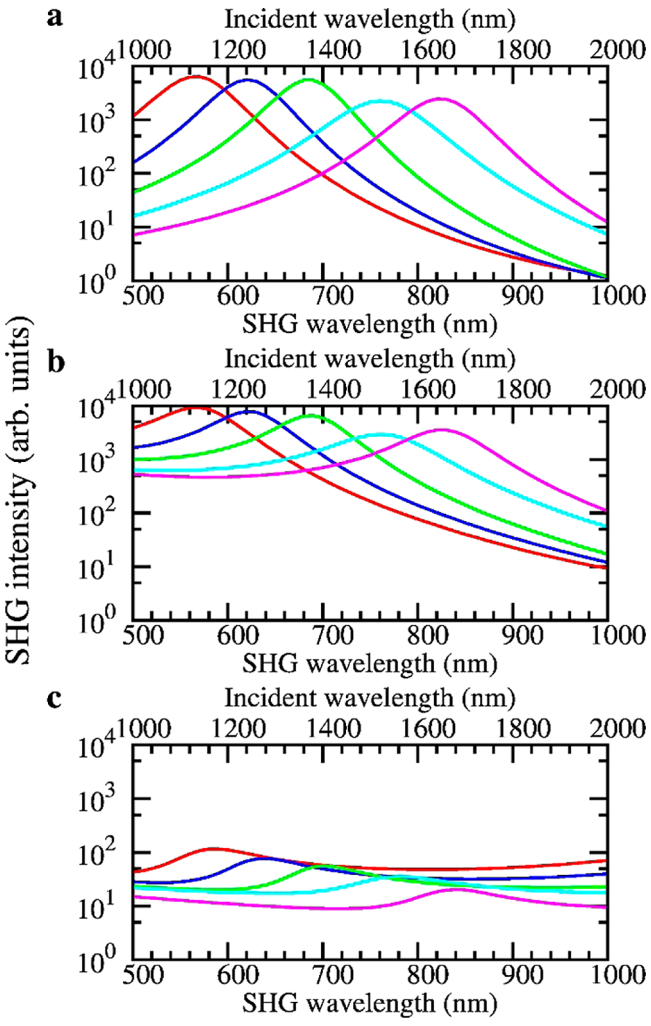


**Figure 7.** Calculated SHG intensity as a function of the incident wavelength for the ITO nanolayers with $\lambda_{ENZ}$ = 1150 (red), 1270 (blue), 1390 (green), 1550 (cyan), and 1670 nm (magenta). The second-order susceptibility components are ($\chi_{zzz}^{(2\omega)} \neq 0$, $\chi_{xzx}^{(2\omega)} = 0$, $\chi_{zxx}^{(2\omega)} = 0$) (a), ($\chi_{zzz}^{(2\omega)} = 0$, $\chi_{xzx}^{(2\omega)} \neq 0$, $\chi_{zxx}^{(2\omega)} = 0$) (b), and ($\chi_{zzz}^{(2\omega)} = 0$, $\chi_{xzx}^{(2\omega)} = 0$, $\chi_{zxx}^{(2\omega)} \neq 0$) (c).

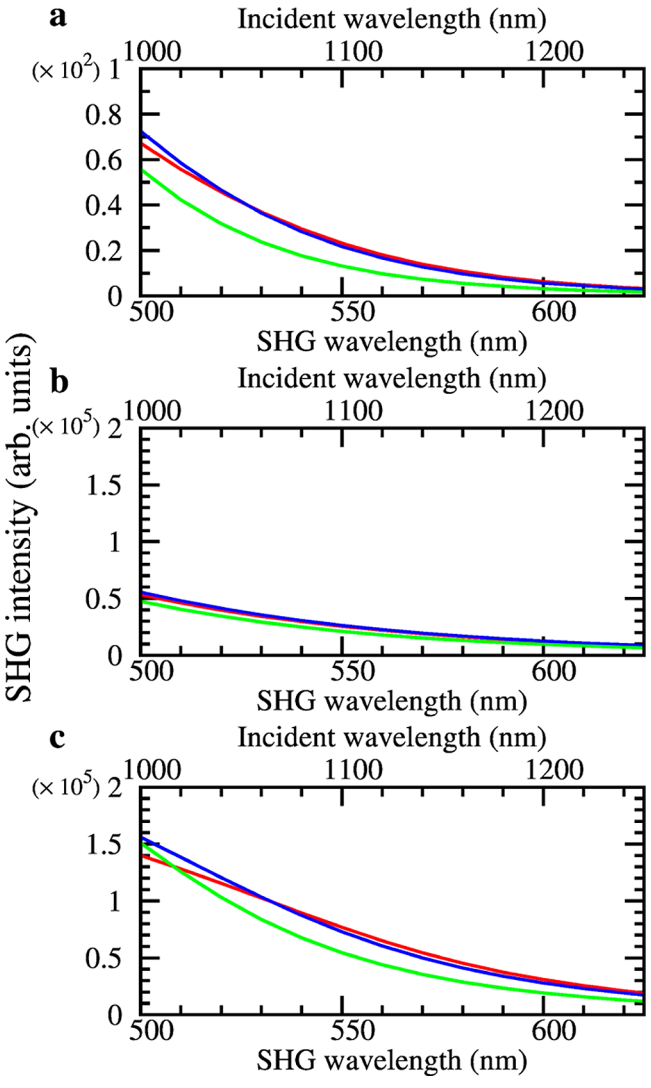


**Figure 8.** Similar to Figure 7, but for the TiN nanolayers with $\lambda_{ps}$ = 510 (red), 545 (blue), and 565 nm (green).



DOI: 10.1021/acsphotonics.5b00355
ACS Photonics 2015, 2, 1584−1591

Figure 8b and ($\chi^{(2\omega)}_{zzz} = 0, \chi^{(2\omega)}_{xzx} = 0, \chi^{(2\omega)}_{zxx} \neq 0$) for Figure 8c. The TiN nanolayers display a metallic behavior in the investigated spectral range. For this reason, the SHG intensity monotonically decreases as the incident wavelength increases for all the investigated components of the second-order susceptibility. It is interesting to note that, assuming equal amplitude for $\chi^{(2\omega)}_{zzz}$, $\chi^{(2\omega)}_{xzx}$, and $\chi^{(2\omega)}_{xzx}$, the SHG intensity due to the $\chi^{(2\omega)}_{zzz}$ component is 3 orders of magnitude lower than the others. This is due to the metallic behavior of the TiN nanolayers in the near-infrared, which negatively affects the extraction of SHG light. Moreover, the second-order polarization induced by $\chi^{(2\omega)}_{zzz}$ depends on the normal component $E_z$ of the electric field at the incident wavelength, which is strongly reduced inside the TiN nanolayers, as already shown in Figure 2c.

In order to quantify the second-order susceptibility of the investigated nanolayers, we performed relative measurements with a reference material, as detailed in Chapter 4 of ref 50. Specifically, we considered the reflected SHG intensity from a *Y*-cut quartz plate of thickness 0.5 mm. We measured the SHG *s*-component $I^{(2\omega)}_{quartz}$ generated by an *s*-polarized incident beam, when the quartz standard axis 1 is parallel to the *s*-direction. We assumed the value $\chi_{111} = 0.6$ pm V$^{-1}$ for the second-order susceptibility of quartz, where the subscripts refer to the standard crystallographic axes.[51] We obtained that the SHG intensity $I^{(2\omega)}_{ITO}$ of the best ITO nanolayer (with $\lambda_{ENZ} = 1150$ nm) is comparable with the quartz plate (our experimental measurements indicated that $I^{(2\omega)}_{ITO}/I^{(2\omega}_{quartz} \approx 1/3.5$), when both are pumped at $\lambda = 1100$ nm. This is a remarkable performance for the ITO nanolayers, considering that the quartz plate thickness is as large as 0.5 mm. As a comparison, in ref 52 the SHG from arrays of silver nanoparticles and islands excited at $\lambda = 1060$ nm resulted to be $\sim 2 \times 10^{-3}$ lower than a quartz sample (with unspecified orientation).[52] By comparing the calculated and the experimental values of the SHG intensity, we estimated that the second-order susceptibility components are $\chi^{(\omega)}_{zzz} = 0.18$ pm V$^{-1}$ and $\chi^{(\omega)}_{xzx} = 0.05$ pm V$^{-1}$ (in good agreement with previous studies[53]) and that the SHG efficiency is $\eta_{SHG} = I^{(2\omega)}/I^{(\omega)} = 3 \times 10^{-13}$ at $I^{(\omega)}_{peak} = 42$ MW/cm$^2$. Since the SHG is a second-order nonlinear process, $\eta_{SHG}$ increases linearly with the incident intensity and the slope has a constant value $\eta_{SHG}/I^{(\omega)}_{peak} = 7 \times 10^{-21}$ cm$^2$/W. As a comparison, the arrays of nanowires investigated in ref 54 have a maximum $\eta_{SHG}/I^{(\omega)}_{peak} = 3.5 \times 10^{-21}$ cm$^2$/W with the excitation at $\lambda = 800$ nm, whereas the nanoantenna recently reported in ref 55 has a maximum $\eta_{SHG}/I^{(\omega)}_{peak} = 2.1 \times 10^{-21}$ cm$^2$/W in the same 940−1480 nm spectral range targeted here (although enhanced values are reported for longer wavelengths). The comparison with the results obtained by other groups is affected by the different experimental conditions, especially the spectral and temporal properties of the excitation beam. However, it is clear from our results that ITO nanolayers provide an excellent nonlinear optical performance even without utilizing surface nanostructuring. This is a direct consequence of the enhanced internal electric field at the ENZ wavelength. For the TiN samples, the SHG efficiency is $\eta_{SHG} = I^{(\omega)}/I^{(\omega)} = 6 \times 10^{-15}$ at $I^{(\omega)}_{peak} = 42$ MW/cm$^2$, with a slope $\eta_{SHG}/I^{(\omega)}_{peak} = 1.4 \times 10^{-22}$ cm$^2$/W. Crystalline TiN is a centrosymmetric medium, and therefore, the bulk second-order susceptibility is zero in the dipolar approximation. The SHG from centrosymmetric conductors is generally attributed to surface effects and to nonlocal bulk effects. The samples investigated here are polycrystalline, and the grain boundaries also play important effects in optical nonlinearities. We attribute the low second-order optical nonlinearity of the fabricated TiN nanolayers to the grain centrosymmetry and to the significant optical losses associated with the large imaginary part of the permittivity.

## CONCLUSIONS

In this work, we experimentally showed that both ITO and TiN nanolayers can be fabricated to have tailorable optical dispersion in the near-infrared. We also theoretically predicted that the SHG process in ITO is enhanced by approximately 4 orders of magnitude if the excitation wavelength matches the ENZ condition of the material. Remarkably, the ITO nanolayers generate an SHG signal of comparable intensity with that of a crystalline quartz plate of thickness 0.5 mm, while TiN show a much lower SHG intensity. In conclusion, ITO is an efficient platform for surface optical nonlinearities, which is compatible with Si fabrication technology and it is applicable for scalable and planar-integrated metamaterial structures.

## AUTHOR INFORMATION

### Corresponding Author

*E-mail: dalnegro@bu.edu.

### Notes

The authors declare no competing financial interest.

## ACKNOWLEDGMENTS

This work was supported by the AFOSR program "Emitters for High Density Information Processing Using Photonic−Plasmonic Coupling in Coaxial Nanopillars" under Award No. FA9550−13−1−0011 and by the NSF EAGER program "Engineering Light−Matter Interaction via Topological Phase Transitions in Photonic Heterostructures with Aperiodic Order" under Award No. ECCS 1541678. A.C. acknowledges the financial support of Italian MIUR through Project PON01 02782. N.E. acknowledges support from the U.S. Office of Naval Research (ONR) Multidisciplinary University Research Initiative (MURI) Grant No. N00014−10−1−0942.

## REFERENCES

(1) Engheta, N.; Ziolkowski, R. W. *Metamaterials: Physics and Engineering Explorations*; Wiley: New York, 2006.
(2) Maier, S. A. *Plasmonics: Fundamentals and Applications*; Springer: New York, 2007.
(3) Schuller, J. a; Barnard, E. S.; Cai, W.; Jun, Y. C.; White, J. S.; Brongersma, M. L. Plasmonics for Extreme Light Concentration and Manipulation. *Nat. Mater.* **2010**, *9*, 193−204.
(4) Silva, A.; Monticone, F.; Castaldi, G.; Galdi, V.; Alù, A.; Engheta, N. Performing Mathematical Operations with Metamaterials. *Science* **2014**, *343*, 160−163.
(5) Yu, N.; Capasso, F. Flat Optics with Designer Metasurfaces. *Nat. Mater.* **2014**, *13*, 139−150.
(6) Della Giovampaola, C.; Engheta, N. *Nat. Mater.* **2014**, *13*, 1115−1121.
(7) Dal Negro, L. Electromagnetic Metamaterials: Simplicity Unlocks Complexity. *Nat. Mater.* **2014**, *13*, 1080−1081.
(8) Cui, T. J.; Qi, M. Q.; Wan, X.; Zhao, J.; Cheng, Q. Coding Metamaterials, Digital Metamaterials and Programming Metamaterials. *Light: Sci. Appl.* **2014**, *3*, e218.
(9) Kauranen, M.; Zayats, A. V. *Nat. Photonics* **2012**, *6*, 737−748.
(10) Cai, W.; Vasudev, A. P.; Brongersma, M. L. Electrically Controlled Nonlinear Generation of Light with Plasmonics. *Science* **2011**, *333*, 1720−1723.
(11) Dionne, J. A.; Diest, K.; Sweatlock, L. A.; Atwater, H. A. PlasMOStor: A Metal-Oxide-Si Field Effect Plasmonic Modulator. *Nano Lett.* **2009**, *9*, 897−902.



DOI: 10.1021/acsphotonics.5b00355
*ACS Photonics* 2015, 2, 1584−1591

(12) Cai, W.; White, J. S.; Brongersma, M. L. Compact, High-Speed and Power-Efficient Electrooptic Plasmonic Modulators. *Nano Lett.* **2009**, *9*, 4403−4411.
(13) Naik, G. V.; Shalaev, V. M.; Boltasseva, A. Alternative Plasmonic Materials: Beyond Gold and Silver. *Adv. Mater.* **2013**, *25*, 3264−3294.
(14) Capretti, A.; Walsh, G. F.; Minissale, S.; Trevino, J.; Forestiere, C.; Miano, G.; Dal Negro, L. Multipolar Second Harmonic Generation from Planar Arrays of Au Nanoparticles. *Opt. Express* **2012**, *20*, 15797.
(15) McMahon, M. D.; Ferrara, D.; Bowie, C. T.; Lopez, R.; Haglund, R. F.; Physics, A. Second Harmonic Generation from Resonantly Excited Arrays of Gold Nanoparticles. *Appl. Phys. B: Lasers Opt.* **2007**, *87*, 259−265.
(16) Walsh, G. F.; Dal Negro, L. Enhanced Second Harmonic Generation from Au Nanoparticle Arrays by Femtosecond Laser Irradiation. *Nanoscale* **2013**, *5*, 7795−7799.
(17) Naik, G. V.; Kim, J.; Boltasseva, A. Oxides and Nitrides as Alternative Plasmonic Materials in the Optical Range. *Opt. Mater. Express* **2011**, *1*, 1090.
(18) Boltasseva, A.; Atwater, H. a. Materials Science. Low-Loss Plasmonic Metamaterials. *Science* **2011**, *331*, 290−291.
(19) West, P. R.; Ishii, S.; Naik, G. V.; Emani, N. K.; Shalaev, V. M.; Boltasseva, A. Searching for Better Plasmonic Materials. *Laser Photonics Rev.* **2010**, *4*, 795−808.
(20) Naik, G. V.; Schroeder, J. L.; Ni, X.; Kildishev, A. V.; Sands, T. D.; Boltasseva, A. Titanium Nitride as a Plasmonic Material for Visible and Near-Infrared Wavelengths. *Opt. Mater. Express* **2012**, *2*, 478−489.
(21) Zhao, H.; Wang, Y.; Capretti, A.; Dal Negro, L.; Klamkin, J.; Member, S. Broadband Electroabsorption Modulators Design Based on Epsilon-Near-Zero Indium Tin Oxide. *IEEE J. Sel. Top. Quantum Electron.* **2015**, *21*, 4.
(22) Wang, Y.; Sugimoto, H.; Inampudi, S.; Capretti, A.; Fujii, M.; Dal Negro, L. Broadband Enhancement of Local Density of States Using Silicon-Compatible Hyperbolic Metamaterials. *Appl. Phys. Lett.* **2015**, *106*, 241105.
(23) Guler, U.; Boltasseva, A.; Shalaev, V. M. Refractory Plasmonics. *Science* **2014**, *344*, 263−264.
(24) Li, W.; Guler, U.; Kinsey, N.; Naik, G. V.; Boltasseva, A.; Guan, J.; Shalaev, V. M.; Kildishev, A. V. Refractory Plasmonics with Titanium Nitride: Broadband Metamaterial Absorber. *Adv. Mater.* **2014**, *26*, 7959−7965.
(25) Raimondi, M. T.; Pietrabissa, R. The in-Vivo Wear Performance of Prosthetic Femoral Heads with Titanium Nitride Coating. *Biomaterials* **2000**, *21*, 907−913.
(26) Ting, C. Y. TiN Formed by Evaporation as a Diffusion Barrier between Al and Si. *J. Vac. Sci. Technol.* **1982**, *21*, 14.
(27) Engheta, N. Pursuing Near-Zero Response. *Science* **2013**, *340*, 286−287.
(28) Silveirinha, M.; Engheta, N. Tunneling of Electromagnetic Energy through Subwavelength Channels and Bends Using E-near-Zero Materials. *Phys. Rev. Lett.* **2006**, *97*, 157403.
(29) Edwards, B.; Alù, A.; Young, M. E.; Silveirinha, M.; Engheta, N. Experimental Verification of Epsilon-near-Zero Metamaterial Coupling and Energy Squeezing Using a Microwave Waveguide. *Phys. Rev. Lett.* **2008**, *100*, 033903.
(30) Silveirinha, M. G.; Engheta, N. Transporting an Image through a Subwavelength Hole. *Phys. Rev. Lett.* **2009**, *102*, 103902.
(31) Ciattoni, A.; Marini, A.; Rizza, C.; Scalora, M.; Biancalana, F. Polariton Excitation in Epsilon-near-Zero Slabs: Transient Trapping of Slow Light. *Phys. Rev. A: At., Mol., Opt. Phys.* **2013**, *87*, 053853.
(32) Alù, A.; Engheta, N. Plasmonic and Metamaterial Cloaking: Physical Mechanisms and Potentials. *J. Opt. A: Pure Appl. Opt.* **2008**, *10*, 093002.
(33) Alù, A.; Engheta, N. Cloaking a Sensor. *Phys. Rev. Lett.* **2009**, *102*, 233901.
(34) Ciattoni, a.; Rizza, C.; Palange, E. Extreme Nonlinear Electrodynamics in Metamaterials with Very Small Linear Dielectric Permittivity. *Phys. Rev. A: At., Mol., Opt. Phys.* **2010**, *81*, 043839.
(35) Vincenti, M. a.; De Ceglia, D.; Ciattoni, a.; Scalora, M. Singularity-Driven Second- and Third-Harmonic Generation at $\varepsilon$-near-Zero Crossing Points. *Phys. Rev. A: At., Mol., Opt. Phys.* **2011**, *84*, 063826.
(36) Ciattoni, a.; Spinozzi, E. Efficient Second-Harmonic Generation in Micrometer-Thick Slabs with Indefinite Permittivity. *Phys. Rev. A: At., Mol., Opt. Phys.* **2012**, *85*, 043806.
(37) Argyropoulos, C.; Chen, P.-Y. Y.; D'Aguanno, G.; Engheta, N.; Alù, A.; D'Aguanno, G.; Engheta, N.; Alù, A. Boosting Optical Nonlinearities in E-near-Zero Plasmonic Channels. *Phys. Rev. B: Condens. Matter Mater. Phys.* **2012**, *85*, 045129.
(38) Vassant, S.; Archambault, a.; Marquier, F.; Pardo, F.; Gennser, U.; Cavanna, a.; Pelouard, J. L.; Greffet, J. J. Epsilon-near-Zero Mode for Active Optoelectronic Devices. *Phys. Rev. Lett.* **2012**, *109*, 237401.
(39) Suchowski, H.; O'Brien, K.; Wong, Z. J.; Salandrino, A.; Yin, X. B.; Zhang, X. Phase Mismatch-Free Nonlinear Propagation in Optical Zero-Index Materials. *Science* **2013**, *342*, 1223−1226.
(40) Vesseur, E. J. R.; Coenen, T.; Caglayan, H.; Engheta, N.; Polman, A. Experimental Verification of $n = 0$ Structures for Visible Light. *Phys. Rev. Lett.* **2013**, *110*, 013902.
(41) Maas, R.; Parsons, J.; Engheta, N.; Polman, A. Experimental Realization of an Epsilon-near-Zero Metamaterial at Visible Wavelengths. *Nat. Photonics* **2013**, *7*, 907−912.
(42) Moitra, P.; Yang, Y.; Anderson, Z.; Kravchenko, I. I.; Briggs, D. P.; Valentine, J. Realization of an All-Dielectric Zero-Index Optical Metamaterial. *Nat. Photonics* **2013**, *7*, 791.
(43) Capretti, A.; Wang, Y.; Engheta, N.; Dal Negro, L. Enhanced Third-Harmonic Generation in Si-Compatible Epsilon-near-Zero Indium Tin Oxide Nanolayers. *Opt. Lett.* **2015**, *40*, 1500.
(44) Wang, Y.; Capretti, A.; Dal Negro, L. Wide tuning of the optical and structural properties of alternative plasmonic materials. *Opt. Mater. Express* **2015**, *5*, 2415−2430.
(45) Palik, E. D. *Handbook of Optical Constants*. Academic Press: New York, 1998.
(46) Chew, W. C. *Waves and Fields in Inhomogenous Media*, IEEE Press Series on Electromagnetic Wave Theory; Wiley: New York, 1999.
(47) Novotny, L.; Hecht, B. *Principles of Nano-Optics*; Cambridge University Press: London, U.K., 2006.
(48) Sipe, J. E. New Green-Function Formalism for Surface Optics. *J. Opt. Soc. Am. B* **1987**, *4*, 481.
(49) Maki, J. J.; Kauranen, M.; Persoons, A. Surface Second-Harmonic Generation from Chiral Materials. *Phys. Rev. B: Condens. Matter Mater. Phys.* **1995**, *51*, 1425−1434.
(50) Sutherland, R. L. Handbook of Nonlinear Optics. *Opt. Eng.* **1997**, *36*, 964.
(51) Boyd, R. W. *Nonlinear Optics*; Elsevier: New York, 2008.
(52) Wokaun, a.; Bergman, J. G.; Heritage, J. P.; Glass, a. M.; Liao, P. F.; Olson, D. H. Surface Second-Harmonic Generation from Metal Island Films and Microlithographic Structures. *Phys. Rev. B: Condens. Matter Mater. Phys.* **1981**, *24*, 849−856.
(53) Wang, W.; Xu, J.; Liu, X.; Jiang, Y.; Wang, G.; Lu, X. Second Harmonic Generation Investigation of Indium Tin Oxide Thin Films. *Thin Solid Films* **2000**, *365*, 116−118.
(54) Belardini, A.; Larciprete, M. C.; Centini, M.; Fazio, E.; Sibilia, C.; Bertolotti, M.; Toma, A.; Chiappe, D.; Buatier de Mongeot, F. Tailored Second Harmonic Generation from Self-Organized Metal Nano-Wires Arrays. *Opt. Express* **2009**, *17*, 3603−3609.
(55) Aouani, H.; Navarro-Cia, M.; Rahmani, M.; Sidiropoulos, T. P. H.; Hong, M.; Oulton, R. F.; Maier, S. a. Multiresonant Broadband Optical Antennas as Efficient Tunable Nanosources of Second Harmonic Light. *Nano Lett.* **2012**, *12*, 4997−5002.


DOI: 10.1021/acsphotonics.5b00355
*ACS Photonics* 2015, 2, 1584−1591